IEEE Access
Multidisciplinary ⋮ Rapid Review ⋮ Open Access Journal

Received October 15, 2020, accepted October 22, 2020, date of publication October 26, 2020, date of current version November 6, 2020.

Digital Object Identifier 10.1109/ACCESS.2020.3033676

Research on Dynamic Test of Hyper-Velocity Impact Penetration Acceleration Signal

DEBIAO ZHANG[1], JIE LI[1,2], XIAOKAI WEI[1], KAIQIANG FENG[1], YU WANG[1], JIHE ZHAO[1], AND DONG XUE[1]

[1]Key Laboratory of Instrumentation Science & Dynamic Measurement, North University of China, Taiyuan 030051, China
[2]National Key Laboratory for Electronic Measurement Technology, North University of China, Taiyuan 030051, China

Corresponding author: Jie Li (lijie@nuc.edu.cn)

This work was supported in part by the National Natural Science Funds for Distinguished Young Scholars under Grant 51225504, in part by the National Natural Science Foundation of China under Grant 51575500 and Grant 51705477, and in part by the Foundation for Middle-Aged and Young Talents in Higher Education Institutions.

ABSTRACT In recent years, with the development of hyper-velocity weapon, the research focus of penetration effect has switched gradually from high-velocity to hyper-velocity, with insufficient studies on penetration effect and its internal mechanism. Besides, the study on penetration effect of hyper-velocity weapon depends on the measurement of mechanical signal during penetration of projectile. In this paper, dynamic test of hyper-velocity impact penetration acceleration signal is studied in depth. Firstly, the penetration velocity and acceleration of projectile under the impact load are analyzed, the influence of the movement of the testing unit on the measured acceleration signal is studied, and the factors to be considered when measuring the hyper-velocity impact load are given. Further, this paper designs a measurement circuit and dynamic models of each measurement module, details the influence of dynamic characteristics of power delivery network on test accuracy, and provides a method to obtain dynamic characteristics of power delivery network by virtue of S parameter. Finally, to extract the real penetration overload signal, a superior noise reduction algorithm adopting Modified Ensemble Empirical Mode Decomposition (MEEMD) is proposed, taking dynamic uncertainty and degree of approximation as evaluation indicators, and the measured sensor data is analyzed and processed with the proposed superior noise reduction algorithm. The experiment results show that, this method has a better noise reduction effect, and can be adopted to effectively extract real penetration overload signal. The results have theoretical research and application value to evaluate the reasonableness and effectiveness of measurement method of hyper-velocity penetration overload signal, and seek for a superior processing method for the noisy penetration overload signal.

INDEX TERMS Impact penetration, hyper-velocity, dynamic test, dynamic uncertainty.

I. INTRODUCTION

In recent years, with the development of hyper-velocity weapon, the research focus of penetration effect has switched gradually from high-velocity to hyper-velocity. The penetration mechanism and failure mode of the latter obviously differ from that of general penetration. At present, there are insufficient studies on penetration effect and internal mechanism of high-velocity and hyper-velocity projectile. Besides, the study on penetration effect of hyper-velocity weapon depends on the measurement of mechanical signal during penetration of projectile. The test system shall be specifically designed according to characteristics of hyper-velocity impact penetration signal to enhance the measurement accuracy and reduce the error. We have studied the measurement problem of general penetration overload signal in the early stage, studied the dynamic design principle of the charge-based sensor projectile penetration overload test system, carried out a detailed theoretical derivation of the dynamic model, and provided the theoretical basis for design. Hence, a comprehensive evaluation of the dynamic uncertainty of the test system is achieved, and finally the feasibility of the method is verified by experiment [1]. Our team also carried out some researches on anti-high overload design, which greatly promoted the research in this paper. Aiming at the high-g launching overload of the guided ammunition,

The associate editor coordinating the review of this manuscript and approving it for publication was Chengpeng Hao.

the semi-strapdown stabilization platform in the shell is easily damaged when only the bearing bears axial high overload, the''counter-top hemisphere'' structure was designed. The inertial measurement system can still work stably and reliably when overload reaches 11000g. The design has engineering application value [2]–[4]. With the development of hyper-velocity weapon, it is imperative to study the dynamic test of the hyper-velocity impact penetration acceleration signal.

Traditional earth-penetrating weapons generally use high-hardness alloy and their ground strike velocity generally do not exceed 1km/s. Therefore, in classical rock penetration theory, the projectile is often assumed to be rigid projectile. The core of theoretical analysis is the resistance function of the projectile, and rigid penetration is the more mature part of penetration theory research. At present, with the advancement of science and technology, the launch velocity of projectile is higher. It is verified in experiment that [5]-[10], when the velocity of projectile increases from normal (900m/s) to high-velocity (1200-1700m/s), the mass erosion of the projectile will occur during the penetration process, which seriously affects the penetration performance of the projectile, even causes the ''reversed reduction'' effect of penetration depth. During recent years, hypersonic technology has entered the substantial technology development stage from concept and principle exploration, and the ground strike velocity of hyper-velocity kinetic weapon reaches 3000-5000m/s. The hyper-velocity impact will occur easily during penetration, which becomes an extremely high temperature and high pressure process caused by the rapid release of kinetic energy. In addition to penetration, cratering effect will occur and strong ground impact effect will be triggered. The effect scope reaches far beyond penetration depth, and is close to shallow-buried explosion [11]–[13]. Its penetration mechanism and failure mode are significantly different from general penetration problem.

The above scholars have done in-depth research on penetration of hyper-velocity projectile. The study on penetration effect and internal mechanism of high-velocity and hyper-velocity projectile to rock is however insufficient. The accurate acquisition of acceleration signal of projectile during penetration plays a decisive role in the research of this kind of problem. The dynamic test of hyper-velocity impact penetration acceleration signal is the premise of studying hyper-velocity penetration effect and its internal mechanism.

Addabbo Tommaso proposed a smart measurement system with improved low-frequency response to detect moving charged debris, to be used for turbomachinery condition monitoring. The postprocessing is based on the theoretical analysis of the physical experiment, assuming to use a first-order high-pass charge amplifier, with the introduction of a fitting model based on the linear combination of Gaussian functions [18]. In this article, the detailed time-domain analysis is mainly conducted to design the measurement system. To minimize the noise issues, various design improvements are performed by power integrity and signal integrity analysis in Young-Jun's research. Static power and dynamic power design are reviewed and improved by DC IR drop and power impedance analysis. Signal integrity design is reviewed and improved by time domain signal wave analysis and PCB (Printed Circuit Board) design modifications [19]. This article focuses on power integrity and signal integrity, failing to provide specific equations for the influence of power integrity on signal noise. System-level signal integrity (SI) and power integrity (PI) problems are taken into account in Jai Narayan's research. System-level simulation of high-speed systems with effect of external environment is described. SI and PI issues with complete analysis of package, board, termination, squid card, and decoupling network are shown. Common problems of simulations-passivity violation, stability, causality, and interoperability, are also discussed [20]. The co-design of power and signal integrity issues on a quad flat non-lead (QFN) package is described in Guan's research. A novel decoupling capacitor is achieved by separating the die pad and footprint, coating a solder mask on the footprint and connecting the footprint to the printed circuit board power plane through a via [21]. In Wojcik's paper the power integrity problems of printed circuit board (PCB) are investigated. Power distribution network (PDN) impedance of a few testing configurations of PCB is numerically analyzed and compared with measurements. The influence of selected parameters of the circuit on PDN impedance is examined [22]. The power integrity is only studied in this paper, but not the influence of power integrity on signal quality.

The above scholars have done in-depth research on power integrity and signal integrity, with focuses on signal and power integrity in digital circuit, and less studies on that of sensitive analog circuit and digital-analog hybrid circuit. This paper emphasizes the influence of dynamic characteristics of power distribution network of digital-analog hybrid circuit on measurement accuracy.

Empirical Mode Decomposition (EMD) is a new signal time-domain decomposition method proposed by Huang et al, which is especially suitable for the analysis of nonlinear and non-stationary time series. Empirical Mode Decomposition (EMD) is a new signal time-domain decomposition method proposed by Huang *et al.* It is especially suitable for the analysis of nonlinear and non-stationary time series. It has strong adaptability and has been widely used in the fields of nonlinear data analysis, spectral signal and mechanical vibration signal analysis [23], [24]. Ensemble Empirical Mode Decomposition (EEMD) is an improved algorithm of EMD, which effectively solves the mixing phenomenon of EMD [25]. Yuxing Li proposed a novel noise reduction technique for underwater acoustic signals based on complete ensemble empirical mode decomposition with adaptive noise (CEEMDAN), minimum mean square variance criterion (MMSVC) and least mean square adaptive filter (LMSAF) [26]. The leading edge of the projectile penetration overload signal is steep and contains a large number of characteristics of the impact response of the installation structure. The acquired signal contains many frequency components

and is non-stationary. Therefore, it is necessary to perform effective analysis and processing on the acquired data. Permutation Entropy is a method for detecting time series and dynamic mutation proposed by Bandt *et al.* It features simple concept, rapid calculation speed, and strong anti-interference ability, which is especially suitable for nonlinear data and has better robustness [27]. Reverse Dispersion Entropy is an algorithm proposed by Yuxing Li. RDE takes PE as its theoretical basis and combines the advantages of dispersion entropy (DE) and reverse permutation entropy (RPE) by introducing amplitude information and distance information [28].

The current studies on penetration effect and internal mechanism of high-velocity and hyper-velocity projectile are insufficient. The accurate acquisition of acceleration signal of projectile during penetration plays a decisive role in the research of this kind of problem. The dynamic test of hyper-velocity impact penetration acceleration signal is performed in this paper, starting from factors influencing measurement accuracy, to analyze hyper-velocity penetration effect and its internal mechanism, consider the influence of movement of test unit on the measured acceleration signal, design measurement circuit, and provide dynamic models of each module. In order to obtain real penetration overload signal, a superior noise reduction algorithm is proposed taking dynamic uncertainty and degree of approximation as evaluation indicators. Finally, this proposed method is verified through experiment. The results have certain theoretical research and application value to evaluate the reasonableness and effectiveness of measurement method of hyper-velocity penetration overload signal, and seek for a superior processing method for the noisy penetration overload signal.

II. TESTING PRINCIPLE FOR PENETRATION PROCESS OF PROJECTILE UNDER HYPER-VELOCITY IMPACT OVERLOAD

A. ANALYSIS ON PENETRATION VELOCITY AND ACCELERATION OF PROJECTILE UNDER HYPER-VELOCITY IMPACT OVERLOAD

The theoretical model of hyper-velocity penetration of rod-shaped projectiles originates from the hydrodynamic theory of high-velocity jet. When the velocity of the projectile is extremely high, and when the contact surface pressure of the projectile is extremely large, the strength of the projectile and the target can be ignored, and the penetration of rod-shaped projectile can be simplified to a shaped charge jet. The pressure balance relationship of the contact surface of the projectile target can be described by the Bernoulli equation proposed by Birkhoff *et al.* [14] as Equation (1).

$$\frac{1}{2}\rho_p\left(v_p-u\right)^2=\frac{1}{2}\rho_t u^2 \tag{1}$$

wherein, v_p is the jet velocity (the tail velocity of the projectile), u is the velocity of the target interface, ρ_p is the jet (projectile) density, and ρ_t is the target density. Assuming that penetration is a steady-state process, the dimensionless penetration depth can be obtained from Equation (1), shown in Equation (2).

$$\frac{h}{L}=\frac{1}{\lambda}=\sqrt{\frac{\rho_p}{\rho_t}} \tag{2}$$

wherein, L is the projectile length. Equation (2) is called as "hydrodynamic penetration limit". It is notable that the above calculation result is often considered as the theoretical limit value of penetration depth of continuous jet and long-rod projectile when the velocity approaches to infinite, however, there is always significant deviation between it and the actual penetration depth under the existing experimental velocity conditions, so the above model should be modified to make it more realistic. When the erosion projectile penetrates, only the contact part of the projectile target is in a fluid state, and the rest is still in a rigid state [15], so the strength characteristics of the projectile and the target actually cannot be ignored. The greatest shortcoming of hydrodynamic theory is that it fails not consider the strength of the material, so it is only suitable for penetration at extremely high velocity. For the semi-fluid penetration stage, the description of the interaction between the projectile targets generally adopts a modified hydrodynamic model. The classic modified hydrodynamics model was first proposed based on the penetration of metal target, including the Alekseevskii-Tate model [16].

The Alekseevskii-Tate model proposed by Alekseevskii and Tate is the most classic theoretical model for the penetration of high-velocity rod-shaped projectile. They introduced the strength of projectile and target material (Y_p and R_t) into Bernoulli equation, and established the hydrodynamic model of penetration calculation combining equations of projectile length variation, penetration and projectile deceleration, shown in Equation (3), (4), (5) and (6).

$$\frac{1}{2}\rho_p\left(v_p-u\right)^2+Y_p=\frac{1}{2}\rho_t u^2+R_t \tag{3}$$

$$\frac{dL}{dt}=-\left(v_p-u\right) \tag{4}$$

$$\frac{dh}{dt}=u \tag{5}$$

$$\frac{dv_p}{dt}=-\frac{Y_p}{\rho_p L} \tag{6}$$

wherein, v_p is the jet velocity (the tail velocity of the projectile), u is the velocity of the target interface, ρ_p is the jet (projectile) density, ρ_t is the target density, L is the projectile length, h is the penetration depth, Y_p and R_t is the material strength of projectile and target. In this model, assuming that only the smaller area of the head of the projectile and the target near the contact surface of the projectile are in fluid state during the penetration of the projectile, and the rest of the projectile is still in rigid state. There are two penetration scenarios according to different combinations of projectile target: when $Y_p < R_t$, the projectile penetrates and erodes until the projectile velocity v_p dropped to the critical velocity; when $Y_p > R_t$, the projectile velocity v_p dropped to the critical velocity, and the remaining projectile

TABLE 1. Initial values of relevant parameters.

TYPE	Range
$V_0(m/s)$	2000
$L(mm)$	500
$\rho_p(g/cm^3)$	17.6
$\rho_t(g/cm^3)$	7.8
$Y_p(GPa)$	1
$R_t(Gpa)$	5.5

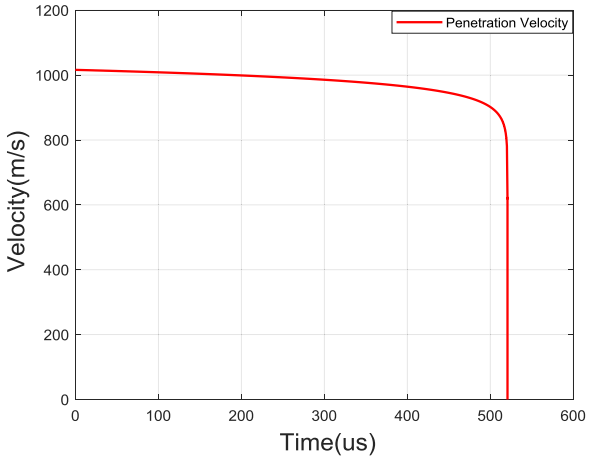

FIGURE 1. The curve of penetration velocity.

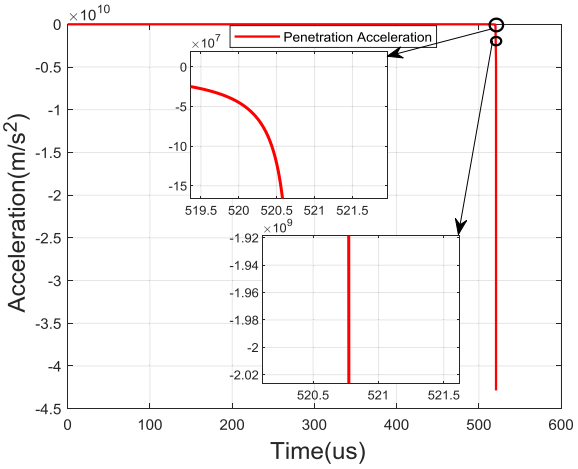

FIGURE 2. The curve of penetration acceleration.

continues to penetrate in rigid-state projectile. For the solution of the Alekseevskii-Tate model, the numerical method is generally adopted. Table 1 shows the test conditions used by Walters *et al.* [17]. According to the test conditions, the numerical solution is performed on Alekseevskii-Tate model, to obtain the curve of penetration velocity and penetration acceleration shown in Fig.1 and Fig.2.

From Fig.1 and Fig.2, the penetration velocity drops sharply during the penetration process, and the falling edge is very steep. The penetration acceleration is obtained by differentiating the penetration velocity, and its variation is even more dramatic. The falling edge of the penetration acceleration signal is even more steep. According to the numerical calculation results of the Alekseevskii-Tate model, the penetration acceleration signal can drop hundreds of thousands of g within $0.01us$. To accurately measure the penetration acceleration signal, according to the sampling theorem, the sampling rate of the data acquisition circuit must be at least 200MHz.

B. ANALYSIS ON INFLUENCE OF TEST UNIT MOVEMENT ON MEASURED ACCELERATION SIGNAL

To accurately measure the penetration process of the projectile, the accelerometer and its data acquisition circuit are required to be placed inside the projectile. The output signal of the accelerometer is the response to the acceleration excitation of its installation point. Therefore, different installations have an influence on the output signal of accelerometer. At present, there are two commonly used installations. One is to install the accelerometer directly on the projectile via bolts. This installation features the highest rigidity and the best frequency response characteristics. However, whether the acceleration sensor is installed on the front end of the projectile or the tail end cover, it is difficult to connect the sensor's data cable and the data acquisition circuit. The other one is to install the circuit module and the accelerometer sensor as a whole part, and then buffer protection should be conducted on the whole part. The purpose is to reduce the connection between the accelerometer sensor and the data acquisition circuit as much as possible, which will greatly improve the impact resistance of the connection line. Hence, the second installation is commonly adopted, whose simplified mechanical mode is show in Fig.3. In Fig.3, c is the damping coefficient of the simplified accelerometer model, k is the elasticity coefficient, and m is the quality.

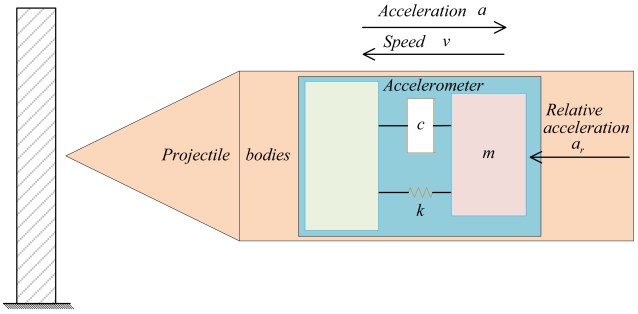

FIGURE 3. Mechanical model of the overall installation of the test unit.

Assuming that the excitation signal of the accelerometer is the basic movement $u = u_0 \sin \omega t$, the basic acceleration is shown in Equation (7)

$$a_f(t) = -u_0\omega^2 \sin \omega t \tag{7}$$

The relatively basic movement equation is Equation (8).

$$m\ddot{x} + c\dot{x} + kx = -ma_f(t) \tag{8}$$

wherein, x is the displacement of the projectile. Equation (7) and (8) are solved, the damping coefficient c is ignored, and the relative displacement is expressed as $1/\omega$ power series. Since the natural frequency of vibration of the acceleration sensor is high, the first three terms are selected, shown in Equation (9).

$$x(t) = -\frac{1}{\omega_n^2}[a_f(t) - a_f(0)\cos\omega_n t - \frac{1}{\omega_n}a_f(0)\sin\omega t] \tag{9}$$

wherein, the first item on the right is the static response of the accelerometer to the inertial force $-ma_f(t)$, and the remaining items are the dynamic response of the accelerometer to the inertial force $-ma_f(t)$, which is a high-frequency signal with a frequency of ω. The latter two items in Equation (9) reflect the influence of high-frequency vibration of the projectile and the installation structure in the measured acceleration signal.

In the projectile penetration experiment, to test the rigid body acceleration $a_f(t)$ of the projectile, it must be extracted from the measured acceleration signal. During the penetration, the sensitive unit of the accelerometer moves forward with acceleration a_r relative to the projectile, and the absolute acceleration sensed by the accelerometer is $a_0 = a_r + a$, which is actually not the acceleration of the projectile. From the perspective of impact response, this problem can be simplified to a second-order system with basic excitation, and the overall equation of movement is Equation (10).

$$m\ddot{y} + c\dot{y} + ky = -m\ddot{x} \tag{10}$$

wherein, y is the displacement of sensitive unit of accelerometer, and x is the displacement of projectile.

$a = \frac{\ddot{x}}{\ddot{x}_{\max}}, \tau = \frac{t}{T}, \delta = -\frac{ky}{m\ddot{x}_{\max}}, R = 2\pi\frac{\sqrt{m/k}}{T}$.Wherein, $\ddot{x}_{\max}$ is the maximum acceleration of the projectile, $\ddot{x}$ is the instantaneous acceleration of the projectile, and T is the duration of the projectile acceleration pulse.

Equation (10) is normalized, and Equation (11) can be obtained.

$$a = \delta + \frac{Rc}{\pi}\frac{d\delta}{d\tau} + (\frac{R}{2\pi})^2\frac{d^2\delta}{d\tau^2} \tag{11}$$

It can be seen from Equation (11) that when R is small, the last two terms of the equation can be ignored, and $\delta = a$. When R becomes larger, the last two terms have obvious effects. The third term causes oscillations up and down in a value, and the second term causes time lag. This will cause change in waveform of the acceleration of the projectile, and the increased error between the penetration velocity and penetration depth obtained by the integration of the acceleration signal and the actual measured value. For any accelerometer sensor, the m and k of its equivalent mechanical models is basically unchanged, so the duration T of the acceleration pulse of the projectile becomes the main factor affecting the measurement accuracy of the penetration acceleration. The smaller the T, the greater the R. That is, during the penetration, the greater the initial velocity of penetration, especially during hyper-velocity impact penetration, the duration of the acceleration pulse of the projectile will be shorter, so that the impact of the latter two items is more obvious. In order to more accurately measure the acceleration during hyper-velocity impact penetration, the influence of the latter two items in Equation (11) is required to be considered.

III. DYNAMIC CHARACTERISTICS DESIGN FOR TEST SYSTEM OF HYPER-VELOCITY IMPACT PENETRATION ACCELERATION SIGNAL

The dynamic characteristics design of the testing system is usually carried out in the frequency domain, to ensure that the system can meet the requirements of the measured signal for the dynamic characteristics. Whether the dynamic characteristics of the testing system can meet the requirements of the measured signal decides the success or failure of the test. And an estimate of the dynamic uncertainty of the system is given. The test system records the variation of the measured signal within the allowable dynamic uncertainty range.

A. DYNAMIC CHARACTERISTICS DESIGN OF TEST CIRCUIT

The sufficient and unnecessary condition for the Fourier transform of the measured signal is that it can satisfy the Dirichlet condition, which is shown in Equation (12).

$$\int_{-\infty}^{+\infty}|x(t)|dt < \infty \tag{12}$$

There are only a finite number of discontinuous points and limit points for $x(t)$ in the interval $t \in (-\infty, \infty)$, and a finite value is taken at the discontinuous point or limit point.

The frequency response characteristics of test system is shown in Equation (13).

$$SYS(f) = A_{senser}(f) \cdot A_{amplifier}(f) \cdot A_{filter}(f) \cdot A_{PDN}(f) \tag{13}$$

wherein, $SYS(f)$ is the frequency response characteristics of system, $A_{senser}(f)$ is that of sensor, $A_{amplifier}(f)$ is that of amplifying circuit, $A_{filter}(f)$ is that of filter, and $A_{PDN}(f)$ is that of power distribution network.

In paper we have published [1], the dynamic test principle of measuring penetration overload signal is studied in detail, providing the frequency response characteristics of sensor $A_{senser}(f)$, that of amplifying circuit $A_{amplifier}(f)$, and that of filter $A_{filter}(f)$. In studying the measurement of hyper-velocity impact penetration acceleration signal, the frequency response characteristics of the power distribution network has a greater impact on the measurement accuracy, which will be discussed in detail in the next section. The accelerometer uses the same sensor, that is piezoelectric accelerometer, with greater range and wider response frequency band. Besides, the structure of the amplifying circuit is also not changed. The sensor is piezoelectric, so a charge amplifying circuit is needed, but the gain of the amplifying circuit is adjusted. Fig.4 is the schematic diagram of the

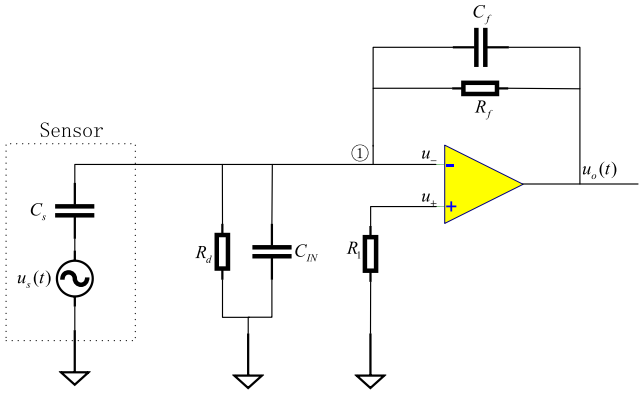

FIGURE 4. The schematic diagram of charge amplifier.

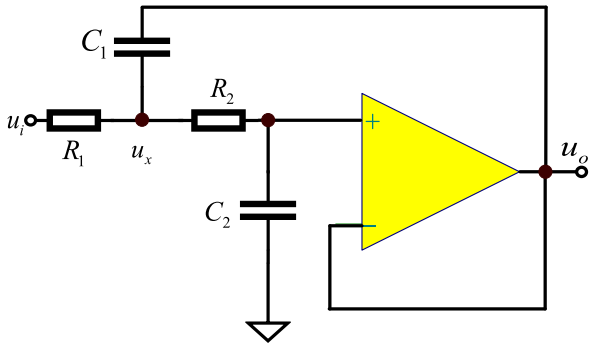

FIGURE 5. The SK low-pass filter circuit diagram.

charge amplifier. The structure of the filter is not changed either. The SK low-pass filter is selected, but the cut-off frequency of the filter is changed. Fig.5 is the schematic diagram of the SK filter. Thus, the frequency response characteristics of these are not changed.

$$A_{sensor}(S) = \frac{\omega_n^2}{S^2 + 2\zeta\omega_n S + \omega_n^2} \tag{14}$$

wherein, ω_n is the undamped oscillation frequency and ζ is the damping coefficient.

$$A_{charge} = \frac{u_o}{Q} = \frac{-1}{\frac{1}{A_{od}}(((A_{od}+1)C_f + C_s + C_{IN}) + \frac{1}{j2\pi f}(\frac{1}{R_d} + (A_{od}+1)\frac{1}{R_f}))} \tag{15}$$

wherein, C_s is the interelectrode capacitance of the sensor, R_d is the parallel value of amplifier input impedance, transmission wire insulation resistance and circuit board insulation resistance, and C_{IN} is the sum of circuit board wire distribution capacitance, cable capacitance and operational amplifier input capacitance. C_f is the feedback capacitor of the charge amplifier, and its value directly determines the gain of the mid-band. R_f is not necessary. It is only to ensure the normal operation of the operational amplifying circuit and avoid the capacitor voltage saturation caused by the continuous paranoid current at the negative input terminal accumulating and charging on the capacitor.

$$A_{fiter}(S) = \frac{1}{1 + SC_2(R_1 + R_2) + S^2C_1C_2R_1R_2} \tag{16}$$

The mutual transformation between the time domain signal and frequency domain can be achieved by fast Fourier transform (FFT) and inverse fast Fourier transform (IFFT). The specific relationship is shown as follows.

The measured signal $x(t)$ is

$$x(t) \xrightarrow{FFT} X(f) \tag{17}$$

The relationship between frequency response characteristics of test system and frequency-domain response of measured signal is shown in Equation (18).

$$R(f) = SYS(f) \cdot X(f) \tag{18}$$

wherein, $SYS(f)$ is the frequency response characteristics of test system, and $R(f)$ is frequency response of measured signal by system. The inverse fast Fourier transform is performed on $R(f)$, and time-domain signal $x_{res}(t)$ output by test system can be obtained and shown in Equation (19).

$$R(f) \xrightarrow{IFFT} x_{res}(t) \tag{19}$$

The dynamic error of the input signal of the test system can be estimated as Equation (20).

$$err(t) = x_{res}(t) - x(t) \tag{20}$$

B. DYNAMIC CHARACTERISTICS DESIGN OF BOARD-LEVEL POWER DISTRIBUTION NETWORK

In the designed hyper-velocity impact penetration acceleration measurement system, the voltage required by various modules is not exactly identical. Generally, the voltage regulator module is used to convert the power into the voltage required by each module. Each module is distributed in different areas on the printed circuit board (PCB), and the power distribution of each module shall be interconnected with cabling, power planes, and via holes on the PCB. The primary and basic requirement for the power distribution network is to maintain the stable power supply voltage between the chip pads to be within an allowable tolerance range. The power distribution network also has impedance, which is not fixed. Under different frequencies, the impedance varies significantly. When the current on the chip fluctuates, the voltage drop will occur on the power distribution network, which is dynamic and related to frequency. The dynamic characteristics of power distribution network has a great influence on measurement accuracy of measurement system. Therefore, it shall be taken into consideration to obtain accurate measurement results.

The impedance of the power distribution network includes resistive impedance, inductive impedance, and capacitive

impedance. The impedance viewed from the chip pad is represented by $Z(f)$, the voltage drop $V(f)$ generated when the current $I(f)$ with a certain spectral width flows through the impedance of the power distribution network is shown in Equation (21).

$$V(f) = I(f)Z(f) \tag{21}$$

This voltage drop on the power distribution network indicates that the stable voltage output by the regulator cannot be obtained by the chip. In order to guarantee the accurate measurement system, this voltage drop must be less than a given maximum threshold. According to the given ripple wave requirement, the maximum allowable impedance of the power distribution network can be solved, shown in Equation (22) and (23).

$$V_{ripple} > V_{PDN} = I(f)Z_{PDN}(f) \tag{22}$$

$$Z_{PDN}(f) < \frac{V_{ripple}}{I(f)} = Z_{MAX\_PDN}(f) \tag{23}$$

wherein, V_{ripple} is the allowable voltage ripple wave, V_{PDN} is the voltage drop of the power distribution network, $I(f)$ is the current flowing through the power distribution network, $Z_{PDN}(f)$ is the impedance of the power distribution network, and $Z_{MAX\_PDN}(f)$ is the maximum allowable impedance of the power distribution network.

In the low frequency range, the voltage regulator module determines the impedance value viewed from the chip to the power distribution network. It, with a reference voltage and a feedback loop, converts a DC voltage into another DC voltage. It detects the voltage in load end, and adjusts the output current to adjust the load voltage. The bandwidth of the regulation loop is usually within a few hundred KHz. At the frequency higher than the bandwidth of the loop, the voltage regulator module becomes high impedance, so the voltage cannot be adjusted effectively. After the bandwidth of the regulation of voltage regulator module is exceeded, the decoupling capacitor on the board plays a decisive role in the impedance of the power distribution network. According to engineering experience, this frequency is usually within hundreds of KHz to 100MHz, which will be the high-frequency limit of the design of board-level power distribution network. When this frequency is exceeded, the impedance of the power distribution network viewed from the chip is only related to the encapsulation and the chip [29]. According to the analysis on penetration velocity and acceleration of projectile under hyper-velocity impact overload, the penetration acceleration drops dramatically, and the falling edge is steep. The penetration acceleration signal can drop hundreds of thousands of g within $0.01us$. To complete the sampling of the penetration acceleration signal, the sampling rate must be at least 200MHz.

We focus on the influence of the dynamic characteristics of the board-level power distribution network on the measurement accuracy. The highest frequency of the board-level power distribution network can be determined by the encapsulated pin inductance, via hole and diffusion inductance. The relationship is shown in Equation (24).

$$Z_{MAX\_PDN} < 2\pi L_{pkg} f_{\max} \tag{24}$$

wherein, Z_{MAX_PDN} is the maximum allowable impedance, L_{pkg} is the equivalent inductance of the encapsulation, and $f_{\max}$ is the highest frequency of the board-level power distribution network.

For designers, the chip and its packaging information are usually difficult to obtain from the supplier, so it is necessary to design board-level decoupling capacitor to ensure that the impedance of the power distribution network is small enough, so the influence of the dynamic characteristics of board-level decoupling capacitor on the measurement accuracy of the test system shall be considered.

The impedance of an ideal capacitor decreases as the frequency increases, but the actual capacitor should be approximated by an RLC circuit model containing equivalent series inductance (ELS) and equivalent series resistance (ESR). The impedance and resonance frequency of the actual capacitor are shown in Equation (25) and (26).

$$Z = R + j\omega L + \frac{1}{j\omega C} \tag{25}$$

$$f_{resonance} = \frac{1}{2\pi\sqrt{LC}} \tag{26}$$

wherein, C is the capacitance of the capacitor, L is the equivalent series inductance of the capacitor, and R is the equivalent series resistance of the capacitor. Fig.6 is the measured impedance of the multilayer ceramic capacitor (MLCC) capacitance of $1uF$.

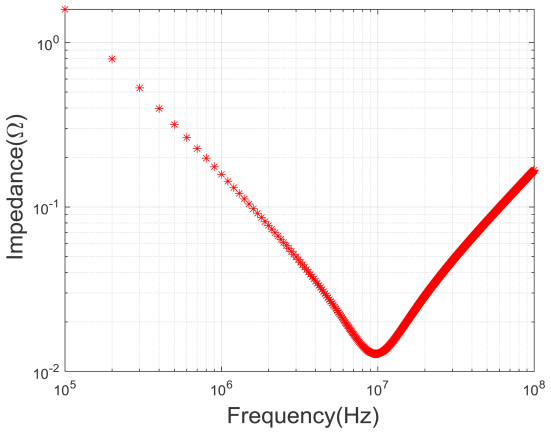

FIGURE 6. The curve of measured impedance of MLCC capacitance of $1uF$.

It can be seen from Fig.6 that the impedance of the actual capacitor mainly depends on the capacitance value at low frequencies, and is mainly determined by the equivalent series inductance (ESL) at high frequencies. The equivalent series resistance (ESR) determines the lower limit of the impedance. In order to enable the impedance of the power distribution network smaller than the design target, it is necessary to select capacitor with appropriate capacitance value and quantity for the power distribution network. Multiple capacitors of

the same power/ground network are connected in parallel. The equivalent capacitance, resistance, and inductance of the same capacitor in parallel connection are shown in Equation (27), (28) and (29), respectively.

$$C_n = nC \tag{27}$$

$$ESR_n = \frac{ESR}{n} \tag{28}$$

$$ESL_n = \frac{ESL}{n} \tag{29}$$

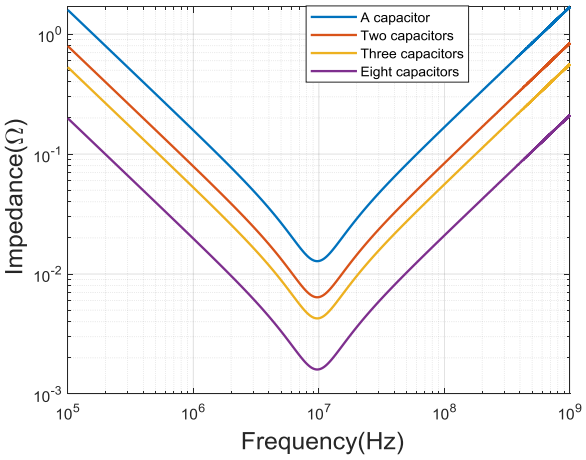

FIGURE 7. The impedance curve of the same capacitors in different numbers connected in parallel.

Fig.7 shows the impedance curve of the same capacitors in different numbers connected in parallel. With the same capacitors are connected in parallel, the frequency of parallel resonance remains unchanged, and the impedance decreases overall. Although the impedance of the power distribution network can be reduced by increasing the number of the same capacitors, the impedance in the frequency range of the point is low only at the resonance frequency point, and the improvement in other frequency bands is not obvious. Therefore, in order to maintain the overall low impedance of the board-level power distribution network, it is necessary to use capacitors with different capacitance value in parallel connection.

Fig.8 presents the impedance curve of two different capacitors in parallel connection. The parameters of the first capacitor are: $C = 1uF$, $ESR = 12.8m\Omega$, $ESL = 0.268nH$. The equivalent series inductance of the second capacitor changes, and the capacitance and equivalent series resistance remain unchanged, so the self-resonant frequency of the second capacitor will change. It can be seen from Fig.8 that when the self-resonant frequencies of the two capacitors are closer, the parallel impedance resonance peak is smaller. When the self-resonant frequencies of the two capacitors are same, the parallel impedance resonance peak disappears. The impedance parallel resonance peak is usually solved by adding a capacitor with a self-resonant frequency between them. Fig.9 shows the impedance variation before and after

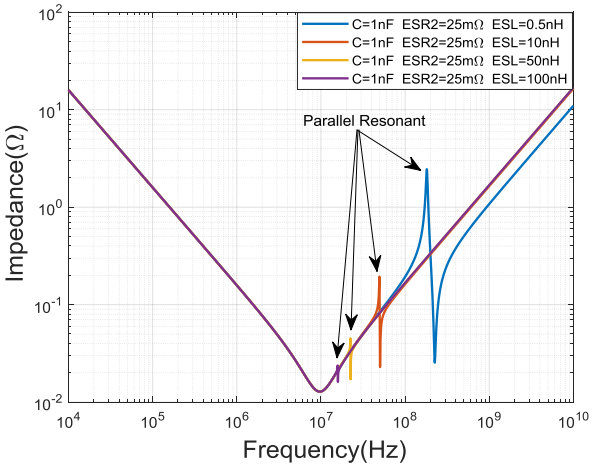

FIGURE 8. The impedance curve of two different capacitors in parallel connection.

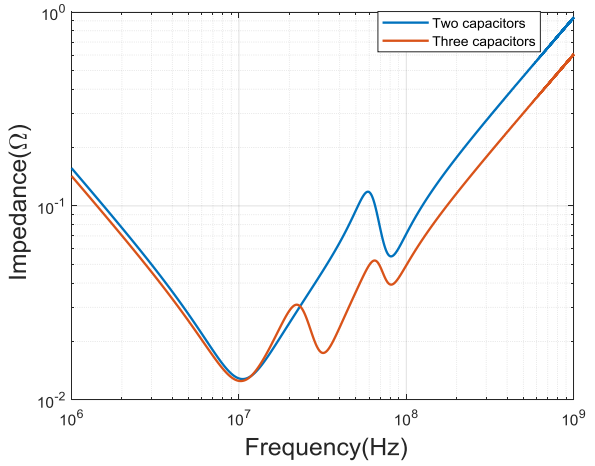

FIGURE 9. The capacitor parallel impedance curve.

adding a capacitor with an intermediate resonant frequency. It can be seen that after adding a capacitor, the parallel impedance resonance peak can be reduced. The capacitance and quantity of capacitors can be determined by the frequency-domain target impedance method created by Larry Smith, which will not be discuss in detail here.

It can be seen from Equation (21) that in order to obtain the dynamic characteristics of the board-level power distribution network, it is necessary to understand the variation rule of its impedance. The current of the chip can be obtained according to the chip manual. In addition to above factors, the impedance of the board-level power distribution network is also related to the location of the decoupling capacitors on the PCB, the way the component is connected, the material of the PCB, the shape of the power supply and the ground plane, and the interconnection of the power supply on the PCB. It can only be solved by the 3D field solver. S parameters of the power distribution network can be extracted via software, or directly measured via a network analyzer, and then the S parameters are converted into Z parameters.

For a circuit with N ports, the incident wave at its nth port is v^+ and the reflected wave is v^-, then,

$$v_n = v^+ + v^- \tag{30}$$

The current is calculated by the port voltage and port impedance Z_n, shown in Equation (31).

$$\mathbf{v} = \mathbf{v}^+ + \mathbf{v}^- = \mathbf{Zi} = \mathbf{Z}\mathbf{v}^+\frac{1}{Z_n} - \mathbf{Z}\mathbf{v}^-\frac{1}{Z_n} \tag{31}$$

wherein, $\mathbf{Z}$ is the impedance matrix, and the scattering matrix can be calculated by solving Equation (31), shown in Equation (32).

$$\mathbf{S} = (\mathbf{v})^+)(\mathbf{v}^-)^{-\mathbf{1}} = (\mathbf{Z} + Z_n\mathbf{U})^{-\mathbf{1}}(\mathbf{Z} - Z_n\mathbf{U}) \tag{32}$$

wherein, $\mathbf{U}$ is the unit matrix, and Z_n is the terminal impedance of each port. Assuming that the terminal value of each port is same, the conversion from S parameter to Z parameter can be obtained according to Equation (32), shown in Equation (33).

$$\mathbf{Z} = Z_n(\mathbf{U} + \mathbf{S})(\mathbf{U} - \mathbf{S})^{-1} \tag{33}$$

To determine whether the design meets the requirements of the required measurement accuracy, it is necessary to evaluate the design in advance, and extract the S parameters of the designed PCB. The extraction of impedance parameters of the power distribution network can be achieved by general software. However, considering that full-wave S parameters can be extracted by a 3D electromagnetic field solver, S parameters are selected to indirectly obtain Z parameters for analysis. Further, the impedance of the power distribution network can be calculated according to Equation (33). In the debugging stage after the PCB is made, the S parameter can be directly measured with a network analyzer to obtain more accurate results.

Fig.10 and Fig.11 are part of the designed PCB. Fig.10 is a power plane of the ADC, with Port2 as the input port of the ADC (Analog to Digital Converter) power distribution network. Fig.11 shows the location distribution of the ADC chip on the Top layer, where Port1 is the power input pin port of the ADC. The Cadence Sigrity software is adopted to extract S parameters between Port1 and Port2. The extracted S11 and S22 parameters are shown in Fig.12 and the extracted S12 and S21 parameters are shown in Fig.13.

After the S parameters are obtained, the conversion relationship between the S parameters and the Z parameters of the two-port can be obtained according to Equation (33), and the Z parameters can be obtained according to Equation (34), as shown at the bottom of the page. Fig.14 is the curve of Z12 and Z21. According to the obtained Z parameters, the least squares method can be used to perform fitting to obtain the relationship $Z(f)$ between impedance and frequency of the power distribution network.

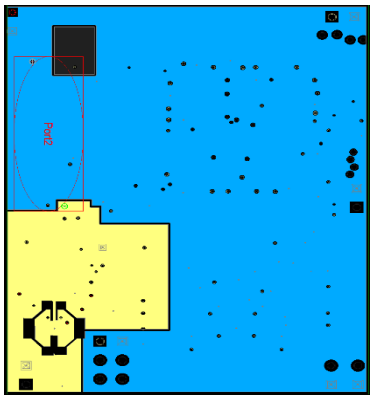

FIGURE 10. The distribution of input ports on ADC power plane.

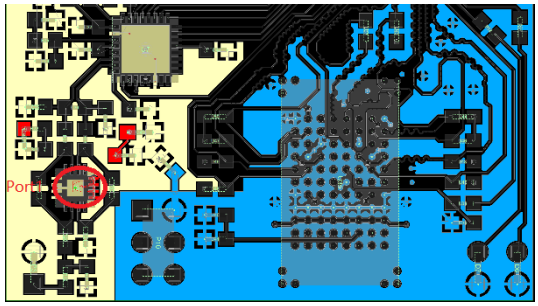

FIGURE 11. The pit location distribution of the ADC chip.

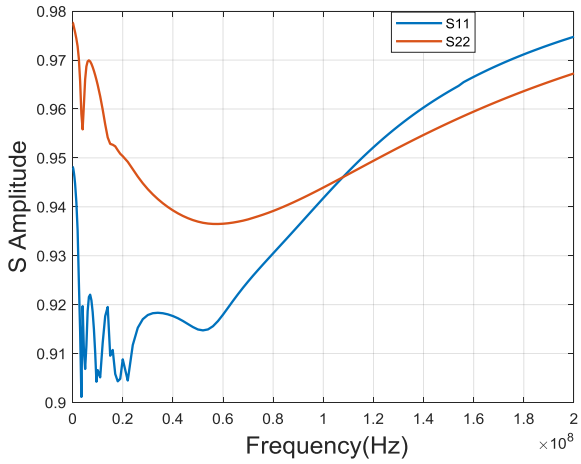

FIGURE 12. The curve of S11 and S22.

$$\begin{bmatrix} Z_{11} & Z_{12} \\ Z_{21} & Z_{22} \end{bmatrix} = \begin{bmatrix} Z_n\dfrac{(1+S_{11})(1-S_{22})+S_{12}S_{21}}{(1-S_{11})(1-S_{22})-S_{12}S_{21}} & \dfrac{2Z_nS_{12}}{(1-S_{11})(1-S_{22})-S_{12}S_{21}} \\ \dfrac{2Z_nS_{21}}{(1-S_{11})(1-S_{22})-S_{12}S_{21}} & Z_n\dfrac{(1-S_{11})(1+S_{22})+S_{12}S_{21}}{(1-S_{11})(1-S_{22})-S_{12}S_{21}} \end{bmatrix} \tag{34}$$

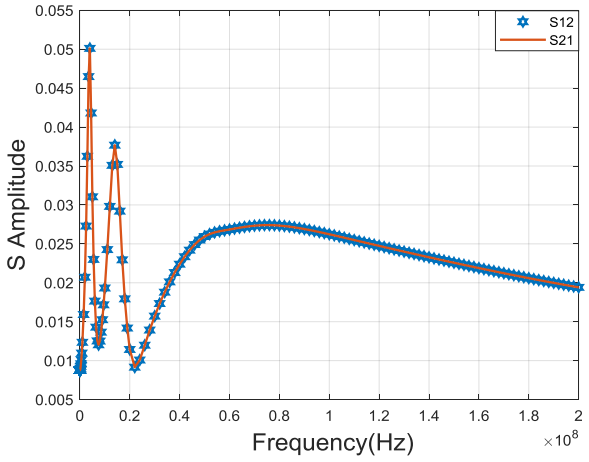

FIGURE 13. The curve of S12 and S21.

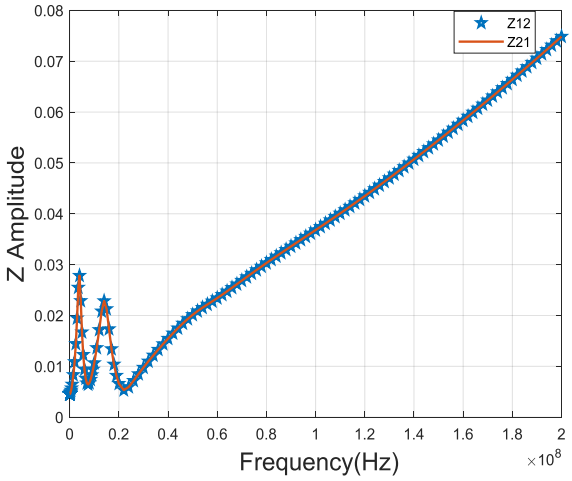

FIGURE 14. The curve of Z12 and Z21.

According to Equation (21), the transfer function of the power distribution network can be obtained and normalized as Equation (35).

$$V_{PDN}(f) = 1 - \frac{V(f)}{V_{VRM}} \tag{35}$$

wherein, $V_{PDN}(f)$ is the transfer function from the input port voltage of ADC power to the pin voltage of ADC power. V_{VRM} is the input voltage of ADC power input port, and $V(f)$ is the voltage drop of the power distribution network.

IV. THE SUPERIOR NOISE REDUCTION ALGORITHM BASED ON MODIFIED ENSEMBLE EMPIRICAL MODE DECOMPOSITION

The hyper-velocity projectile penetration overload signal contains not only the projectile penetration signal, but also the acceleration signal caused by the strong impact effect triggered by the crater effect, as well as the impact sound of the installation structure. Its penetration mechanism and failure mode are significantly different from that of general penetration. In order to accurately obtain the real penetration overload signal, a superior noise reduction algorithm based on Modified Ensemble Empirical Mode Decomposition (MEEMD) is proposed in this paper. Penetration overload signal is a dynamic mutation. Permutation entropy (PE) is a method proposed by Bandt *et al.* to detect randomness in time series and dynamic mutations [27]. RDE has better performance in detecting abrupt signal and noise robustness testing, and has better stability for sensor signal, and a good ability to detect mutation signals [28]. Therefore, RDE is used as a criterion for detecting the penetration overload signal. The Intrinsic Mode Function (IMF) is obtained by decomposition based on the EEMD algorithm, and the RDE of each intrinsic mode function is calculated. Whether the IMF component is a penetration overload signal is determined according to the entropy value. Different filters are constructed, and the superior noise reduction algorithm for penetration overload signal is established. Besides, the judgment criterion of superior noise reduction algorithm is formed based on dynamic uncertainty and approximation index. In view of the great differences in the dynamic characteristics of each frequency band of the board-level power distribution network, a segmented calculation method is adopted in this paper to achieve a comprehensive evaluation of the dynamic uncertainty of the test system.

A. ESTIMATION OF DYNAMIC UNCERTAINTY OF DYNAMIC TEST SYSTEM

The dynamic measurement error of the dynamic test system is generally expressed by the dynamic uncertainty. In order to obtain the measurement accuracy of the designed dynamic test system, it is necessary to correctly estimate the dynamic uncertainty of the designed system.

The amplitude-frequency response characteristic of the test system is shown in Equation (36).

$$A_{SYS}(f) = A_{sen}(f) \cdot A_{ch\arg e}(f) \cdot A_{filter}(f) \cdot A_{PDN}(f) \tag{36}$$

The phase-frequency response characteristic of the test system is shown in Equation (37).

$$\varphi_{sys}(f) = \varphi_{sen}(f) + \varphi_{ch\arg e}(f) + \varphi_{filter}(f) + \varphi_{PDN}(f) \tag{37}$$

The output of the signal $x(t)$ through the actual system is $y_r(t)$, and the output through the ideal distortion-free system is $y_i(t)$, then the dynamic error of the system is:

$$\varepsilon(t) = y_r(t) - y_i(t) \tag{38}$$

When the error is limited energy and limited power, the total energy of dynamic error and the average power of dynamic error are:

$$W_\varepsilon = \int_{-\infty}^{\infty} \varepsilon^2(t)dt \tag{39}$$

$$P_\varepsilon = \lim_{T\to\infty} \frac{1}{2T} \int_{-\infty}^{\infty} \varepsilon^2(t)dt \tag{40}$$

$\sqrt{P_\varepsilon}$ is called dynamic root mean square error or dynamic error effective value. For a time-limited signal $x(n)$ of

duration T_0, the average power of error is:

$$P_{\varepsilon d} = \frac{W_\varepsilon}{T_0} = \frac{1}{T_0}\int_{-\infty}^{\infty} \varepsilon^2(t)dt \tag{41}$$

According to Pasval theorem, there is:

$$P_\varepsilon = \overline{\varepsilon^2} = \int_{-\infty}^{\infty} G_\varepsilon(\omega)df \tag{42}$$

The frequency response function of the ideal system is $H_i(j\omega)$, the actual system is $H_i(j\omega) + \Delta H(j\omega)$, and the power spectral density of the signal is $G_x(j\omega) = |X(j\omega)|^2$. The dynamic error is caused by deviation from the ideal system $\Delta H(j\omega)$:

$$G_\varepsilon(\omega) = G_x(j\omega) \cdot |\Delta H(j\omega)|^2 \tag{43}$$

The power spectrum of error is:

$$P_{\varepsilon d} = \frac{W_\varepsilon}{T_0} = \frac{1}{T_0}\int_{-\infty}^{\infty} |X(j\omega)|^2 |\Delta H(j\omega)|^2 df \tag{44}$$

There are the following method to solve $\Delta H(j\omega)$:

$$H_r(j\omega) = K_r(\omega)e^{j\varphi_r(\omega)} \tag{45}$$

wherein, $K_r(\omega)$ is the amplitude-frequency characteristic of the actual system, $K_r(\omega) = |H_r(j\omega)|$, and $\varphi_r(\omega)$ is the phase-frequency characteristic of the actual system. The frequency characteristic of the ideal system is:

$$H_i(j\omega) = K_i e^{j\varphi_i(\omega)} \tag{46}$$

The amplitude-frequency characteristic of the ideal system in the working frequency band is a constant value. $\varphi_1(\omega)$ is the phase-frequency characteristic of the ideal system. The relationship between the amplitude-frequency characteristic and the phase-frequency characteristic of the ideal system and the actual system are:

$$\Delta\varphi(\omega) = \varphi_r(\omega) - \varphi_i(\omega) \tag{47}$$

$$\Delta K(\omega) = K_i - K_r(\omega) \tag{48}$$

On the Nyquist diagram, $H_r(j\omega)$, $H_i(j\omega)$ and $\Delta H(j\omega)$ form a triangle, and the included angle of $H_r(j\omega)$ and $H_i(j\omega)$ is $\Delta\varphi(\omega)$. From the law of cosines:

$$|\Delta H(j\omega)|^2 = K_r^2 + K_i^2 - 2K_iK_r\cos(\Delta\varphi(\omega)) \tag{49}$$

Substitute Equation (48) into Equation (49), and obtain,

$$|\Delta H(j\omega)|^2 = 2[(K_r(\omega))^2 + K_r(\omega)\cdot\Delta K(\omega)] \cdot(1-\cos(\Delta\varphi(\omega))) + (\Delta K(\omega))^2 \tag{50}$$

Although the interconnected power distribution network is a complex structure, it can be simply divided into three simple sectors in the frequency domain. In the lowest frequency band, the voltage regulator module plays a decisive role in the power distribution network within its own adjustment range. The next higher frequency band is the bulk decoupling capacitor which plays a decisive role in the power distribution network. The dynamic characteristics of the power distribution network in the highest frequency band mainly depends on the on-chip capacitance and the capacitance and equivalent series inductance in the packaging. So the calculation is performed based on sectors:

$$P_\varepsilon = \sum_{f=0}^{f_{VRM}} |\Delta X_{LC}(j\omega)|^2\Delta f + \sum_{f=f_{VRM}}^{f_{BCAP}} |\Delta X_{MC}(j\omega)|^2\Delta f + \sum_{f=f_{BCAP}}^{f_m} |\Delta X_{HC}(j\omega)|^2\Delta f \tag{51}$$

wherein, f_{VRM} is the maximum adjustable frequency of the voltage regulator module, f_{BCAP} is the maximum frequency at which the bulk capacitor works, Δf is the smallest frequency step, $\Delta X_{LC}(j\omega)$ is the vector difference of the frequency characteristics of the low frequency band, $\Delta X_{MC}(j\omega)$ is the vector difference of the frequency characteristics of the mid frequency band, and $\Delta X_{HC}(j\omega)$ is the vector difference of the frequency characteristics of the high frequency band.

B. THE DESIGN OF THE SUPERIOR NOISE REDUCTION ALGORITHM

After the noisy penetration overload signal $y_r(t)$ obtained by the system is decomposed by EEMD, the reconstructed signal can be expressed as:

$$y_r(t) = \sum_{i=1}^{n} IMF_i(t) + r_n(t) \tag{52}$$

wherein, $IMF_i(t)$ is the intrinsic modal function; $r_n(t)$ is the remainder; n is the number of intrinsic modal functions. The RDE of $IMF_i(t)$ is calculated as

$$H_i = F_{PE}(IMF_i(t)) \tag{53}$$

wherein, H_i is the RDE of the intrinsic modal functions, F_{PE} is the function for calculating the sequence RDE, and the specific calculation method can be found in Ref [23]. If $H_L < H_i < H_H$, we think that this intrinsic mode component is a sudden penetration signal,and this inherent modal function is considered as a mutational penetration signal, where H_L is the set lower limit of the threshold and H_H is the set upper limit of the threshold. The specific value should be calibrated according to the system. Separate the intrinsic mode function that meets $H_L < H_i < H_H$ to obtain.

$$r(t) = y_r(t) - \sum_{j=1}^{n} IMF_j(t) \tag{54}$$

wherein, $IMF_j(t)$ is the intrinsic mode function when the entropy value meets $H_L < H_i < H_H$, and n is the number of mode functions when the entropy value meets $H_L < H_i < H_H$. Continue to perform EEMD decomposition on $r(t)$, and further separate the corresponding mode functions until the entropy value of the intrinsic mode functions of $r(t)$ does not meet $H_L < H_i < H_H$.

Add all mode functions that meet $H_L < H_i < H_H$ to form a filter, as shown in Equation (55).

$$LP = \sum_{j=1}^{m} IMF_j(t) \tag{55}$$

wherein, m is the total number of all mode functions when the entropy value meets $H_L < H_i < H_H$, H_L and H_H is the key to determining the filtering performance of the filter, which shall be determined by calibration experiment. This paper adopts the calibration test method based on the Hopkinson rod, and takes the signal measured by the laser interferometer as the standard signal. The specific experiment process is described in detail in the experiment part.

The noisy penetration overload signal measured by the system is written as:

$$y_r = (y_{r1}, y_{r1}, \cdots, y_{rm}) \tag{56}$$

The mean square error of the noise reduction deviation of the algorithm is defined as:

$$MES_f = \sqrt{\frac{\sum_{j=1}^{m} (\hat{y_{rj}} - y_{rj})^2}{m}} \tag{57}$$

wherein, y_{rj} is the noisy penetration overload signal measured at moment $j = 1, 2, \cdots, m$; m is the total number of sampled signals; $\hat{y_{rj}}$ is the result obtained by the algorithm after denoising the signal measured by the test system, $j = 1, 2, \cdots, m$.

Considering MSE_f being equal to zero, the reciprocal of $(MSE_f + 1)$ is called the algorithm approximation degree and written as MSE_f^{-1}. It can be seen that $0 < MSE_f^{-1} \leq 1$, the smaller the mean square error of the noise reduction deviation MSE_f, the closer the MSE_f^{-1} to 1, and the closer the noise reduction result is to the original signal.

The signal measured by the Hopkinson rod laser interferometer is written as:

$$y_i = (y_{i1}, y_{i1}, \cdots, y_{in}) \tag{58}$$

The signal measured by the laser interferometer is considered as the ideal standard signal. According to the method introduced above, solve the dynamic uncertainty of the noisy penetration overload signal obtained by the system.

In terms of the noise reduction of the penetration overload signal, not only the noise reduction effect should be taken into consideration, but also whether the waveform after noise reduction is closely related to the real signal. The smaller the estimated dynamic uncertainty $\sqrt{p_\varepsilon}$, the closer the result after noise reduction to ideal penetration overload signal.

It is expected that the result after noise reduction is sufficiently similar to the ideal penetration overload signal (the smaller the dynamic uncertainty $\sqrt{p_\varepsilon}$, the better, but the greater the $\frac{1}{\sqrt{p_\varepsilon}}$ the better). At the same time, a better noise reduction effect is also required (that is, the greater the algorithm approximation MSE_f^{-1} the better). However, the actual situation is that it is difficult to meet these two indicators at the same time, so the criteria for establishing a superior noise reduction algorithm are as follows:

Constraint conditions

$$\begin{cases} \max\left\{\frac{1}{\sqrt{p_\varepsilon}}\right\} \\ \max\left\{MSE_f^{-1}\right\} \end{cases} \tag{59}$$

The objective function of noise reduction algorithm f is:

$$\max\{f\} = \max\left\{\frac{\alpha}{\sqrt{p_\varepsilon}} + (1-\alpha)\left|MSE_f^{-1}\right|\right\} \tag{60}$$

wherein, α, $1-\alpha$ are the influencing factor of the algorithm dynamic uncertainty and the approximation, whose weights are determined according to the specific requirements of signal processing. After α, $1-\alpha$ are determined, according to the objective function f, the genetic algorithm is used to solve the optimal H_L and H_H. The application of the genetic algorithm will not be discussed in detail in this paper.

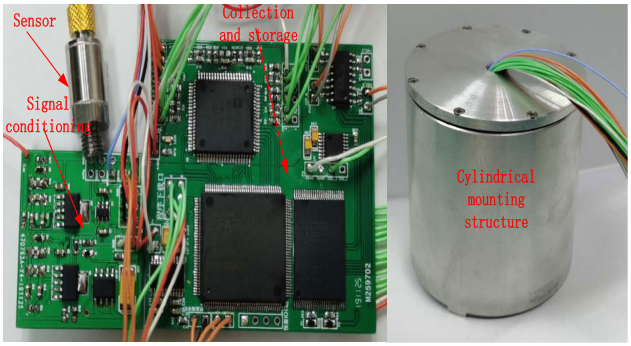

FIGURE 15. Test circuit board.

V. EXPERIMENTAL RESULTS

According to the method in the article, design the test circuit and select the device. The completed circuit board is shown in Fig.15. It is mainly composed of impact sensor, signal conditioning circuit, acquisition and storage circuit, and batteries. In order to improve the impact resistance of the system and shorten the connection between modules, the sensor and each circuit module are installed in a cylindrical structure, glue is used for encapsulation, and the cylindrical structure is installed inside the projectile for test.The 21110 from Shanghai B&W Sensing Technology Co.Ltd with a measuring range of 100000g and a sensitivity of $0.2pC/g$ is adopted. The ADC in the measurement system uses ADI's AD7768 with a resolution of 24bits. The measurement accuracy of the measurement circuit to the electric charge can reach $0.05pC/g$, which can meet the requirements of the selected sensor for the measurement circuit. However, in practical applications, due to the installation method of the sensor and testing system, the actual measurement accuracy is required to be calibrated and tested. Besides, the measurement accuracy of the testing system is given via the following calibration experiment.

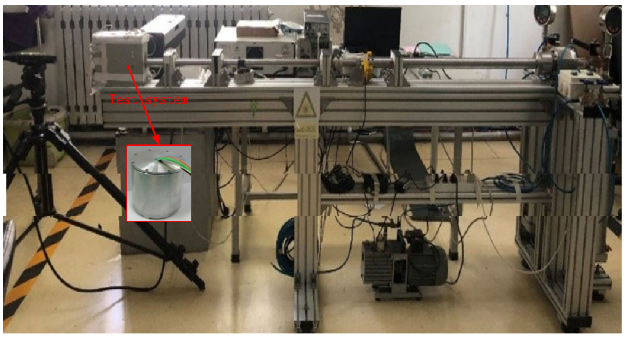

FIGURE 16. Calibration test based on Hopkinson rod.

Fig.16 is the calibration test based on Hopkinson rod. During this experiment, the Hopkinson rod is made of titanium alloy with a diameter of 16mm and a length of 1600mm. The waveform adjustment pad and the acceleration mounting base are tightly sucked on both ends of the Hopkinson rod via industrial silicone grease and vacuum fixtures. The grating is pasted on the cylindrical surface of the accelerometer mounting base as the diffraction cooperation target of the laser interferometer. The bullet hits the waveform adjustment pad on the right side of the Hopkinson rod under the action of compressed air, generating elastic stress pulse and propagating to the left along the Hopkinson. The compression pulse will be reflected on the free end surface of the sensor mounting base as stretching pulse. When the compression pulse and the reflected stretching pulse are superimposed, static tension occurs at the interface between the Hopkinson rod and the accelerometer mounting base, the sensor flies away from the Hopkinson rod, and the laser interferometer uses the diffraction grating attached to the mounting base as the cooperative target to measure the excitation acceleration. The output signal of the sensor will be recorded by the system. By changing the pressure of compressed air, the shape of the bullet head and the material of the adjustment pad, excitation acceleration pulses of different amplitudes and pulse widths can be generated.

Fig.17 is the sensor output signal measured by the designed system. It can be seen that the peak excitation acceleration measured by the designed system is 82797g, the pulse width is 6.27us, and the measured signal contains a great amount of noise. Fig.18 shows the test data curve of the laser interferometer. It can be seen that the acceleration peak value measured by the laser interferometer is 80161g and the pulse width is 6.04us. The signal measured by the laser interferometer is considered as the standard signal, and the effective acceleration signal can be extracted by the superior noise reduction algorithm based on Modified Ensemble Empirical Mode Decomposition (MEEMD), as shown in Fig.19. The result of data processing with the excellent noise reduction algorithm based on Modified Ensemble Empirical Mode Decomposition (MEEMD) proposed in this article is close to the result measured by the laser interferometer. The data processed by the Butterworth digital filter is quite different

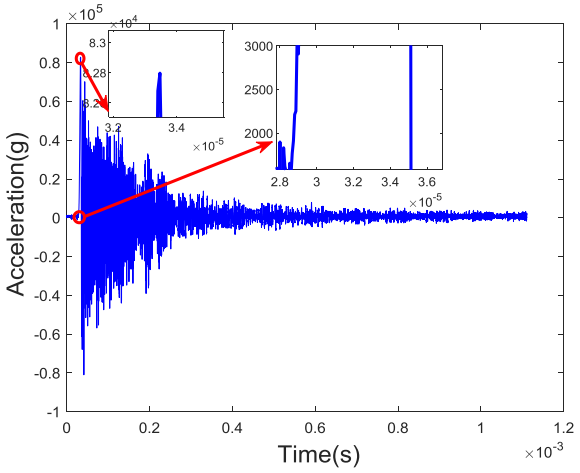

FIGURE 17. The acceleration signal measured by the designed system.

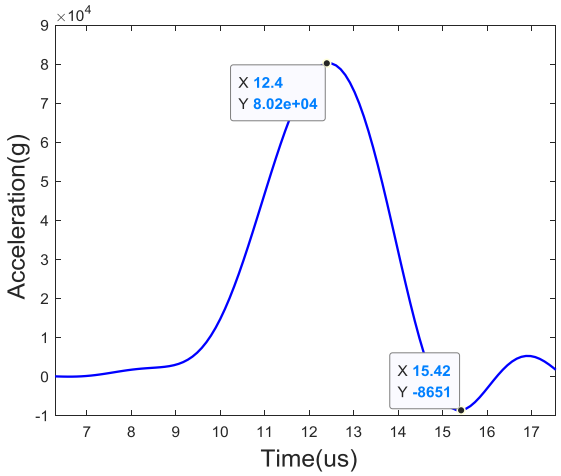

FIGURE 18. The curve of test data of laser interferometer.

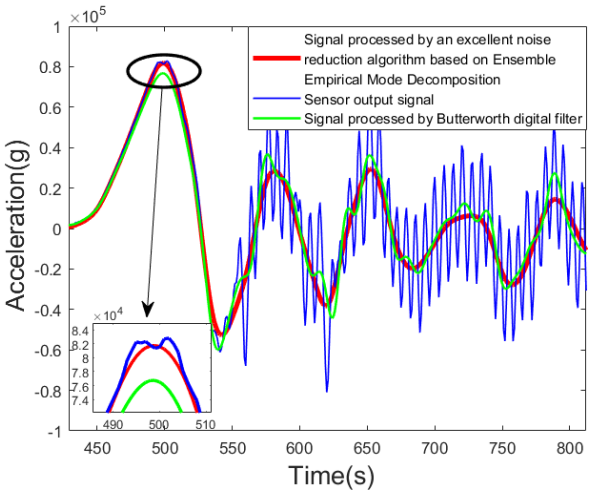

FIGURE 19. Sensor output signal and signal processed by an excellent noise reduction algorithm based on MEEMD.

from the results measured by the laser interferometer. The measured peak value of the impact acceleration is different by 5000g. For the measurement of the impact acceleration,

the first peak plays a decisive role. The data error is too large after processing by the Butterworth digital filter. It can be seen from Fig.18 that after being processed by the excellent noise reduction algorithm proposed in this article, the noise is greatly suppressed, and a good noise reduction effect is realized. It can be calculated that the peak value error of the test circuit to the impact acceleration measurement is 3.29%, and the pulse width error is 3.81%, which also proves the effectiveness of the method proposed in this article.

VI. CONCLUSION

The dynamic test of hyper-velocity impact penetration acceleration signal is performed in this paper. Firstly, the penetration velocity and acceleration of projectile under hyper-velocity impact overload is analyzed. Its penetration mechanism and failure mode are significantly different from that of general penetration. The penetration velocity drops sharply during the penetration process, and the falling edge is very steep. The penetration acceleration is obtained by differentiating the penetration velocity, and its variation is even more dramatic. The falling edge of the penetration acceleration signal is even more steep. According to characteristics of hyper-velocity impact penetration, this paper further studies the influence of movement of test unit on the measured acceleration signal, and gives the factors to be considered when measuring the hyper-velocity impact penetration.

In order to accurately measure the hyper-velocity impact penetration process, according to the characteristics of the hyper-velocity impact penetration acceleration signal, a measurement circuit is designed, and dynamic models of the sensor, amplifying circuit, filter circuit, and power distribution network are given. This paper focuses on the influence of dynamic characteristics of power distribution network on test accuracy, considering the influence of voltage stabilizing module and decoupling capacitor on the impedance of power distribution network, and presents a method to obtain the dynamic characteristics of power distribution network by S parameters, thus determining the influence of dynamic characteristics of power distribution network on that of the entire test system. This article fails to consider the crosstalk among the various signals on the circuit board for the modeling of the measurement circuit. Crosstalk is also a factor that affects the measurement accuracy. This article focuses on the dynamic characteristics of the power distribution network. The power supply is regarded as an ideal power supply, but the actual power supply is noisy, and the noise of the power supply is also a factor that affects the measurement accuracy.

In order to evaluate dynamic characteristics of this type of test system more objectively, the unevenness of the amplitude-frequency characteristics of the test system and its width in frequency domain are not simply considered as the criteria for evaluating dynamic characteristics of the system, but dynamic uncertainty estimation of the measured acceleration signal. In view of the great differences in the dynamic characteristics of each frequency band of the board-level power distribution network, a segmented calculation method is adopted in this paper to achieve a comprehensive evaluation of the dynamic uncertainty of the test system. In order to accurately obtain the real penetration overload signal, a superior noise reduction algorithm based on Modified Ensemble Empirical Mode Decomposition (MEEMD) is proposed in this paper. The Intrinsic Mode Function (IMF) is obtained by decomposition based on the EEMD algorithm, and the RDE of each intrinsic mode function is calculated. Whether the IMF component is a penetration overload signal is determined according to the entropy value. Different filters are constructed, and the superior noise reduction algorithm for penetration overload signal is established. Further, the measured sensor data is analyzed by the proposed superior noise reduction algorithm. The experimental results show that this method has a better noise reduction effect to effectively extract real penetration overload signal. Although the data processing method proposed in this article can suppress mode mixing to a certain extent, the amount of calculation is still large and cannot meet the real-time requirement.

This paper deeply studies dynamic test of hyper-velocity impact penetration acceleration signal. The results have theoretical research and application value to evaluate the reasonableness and effectiveness of measurement method of hyper-velocity penetration overload signal, seek for a superior processing method for the noisy penetration overload signal, and promote the studies on penetration effect and its internal mechanism of hyper-velocity.

REFERENCES

[1] D. Zhang, J. Li, X. Wei, K. Feng, Y. Wang, and J. Zhao, "Signal measurement of projectile penetration overload based on charge sensor," *IEEE Access*, vol. 7, pp. 178139–178152, 2019, doi: 10.1109/access.2019.2958387.
[2] X. Wei, J. Li, T. Zheng, X. Zhang, K. Feng, and H. Qian, "Design of anti-high-overload structure of passive semi-strapdown stabilization platform," *Baozha Yu Chongji/Explosion Shock Waves*, vol. 39, no. 7, 2019.
[3] X. Wei, J. Li, K. Feng, X. Zhang, J. Li, and Z. Lu, "Optimum design and analysis of anti-high-overload structure of roll stabilized platform," *Zhongguo Guanxing Jishu Xuebao/J. Chin. Inertial Technol.*, vol. 26, no. 5, pp. 603–609, 2018.
[4] J. Li, J. Li, L. Qin, W. Liu, X. Wei, N. Gao, and Y. Liu, "Optimal design and analysis on high overload buffer structure of passive semi-strapdown inertial navigation system," *Sensors*, vol. 20, no. 4, p. 1131, Feb. 2020.
[5] Q. Bing-Wen, G. Zhou, J. Li, and D.-Z. Zhang, "Study of the crater produced by hypervelocity tungsten alloy projectile into concrete target," *Trans. Beijing Inst. Technol.*, vol. 38, no. 10, pp. 1012–1017, 2018.
[6] X. Z. Kong, H. Wu, Q. Fang, W. Zhang, and Y. K. Xiao, "Projectile penetration into mortar targets with a broad range of striking velocities: Test and analyses," *Int. J. Impact Eng.*, vol. 106, pp. 18–29, Aug. 2017.
[7] M. J. Forrestal, D. J. Frew, S. J. Hanchak, and N. S. Brar, "Penetration of grout and concrete targets with ogive-nose steel projectiles," *Int. J. Impact Eng.*, vol. 18, no. 5, pp. 465–476, Jul. 1996.
[8] H. E. Xiang, X. U. Xiang-Yun, S. Gui-Juan, S. Jun, Y. Jian-Chao, and J. Dong-Liang, "Experimental investigation on projectiles' high-velocity penetration into concrete targets," *Explosion Shock Waves*, to be published.
[9] Z. Mu and W. Zhang, "An investigation on mass loss of ogival projectiles penetrating concrete targets," *Int. J. Impact Eng.*, vol. 38, nos. 8–9, pp. 770–778, Aug. 2011.
[10] W. Mingyang, Q. Yanyu, L. I. Jie, L. I. Haibo, and Z. Zhangyong, "Theoretical and experimental study on penetration in rock and ground impact effects of long rod projectiles of hyper speed," *Chin. J. Rock Mech. Eng.*, to be published.
[11] T. H. Antoun, L. A. Glenn, O. R. Walton, P. Goldstein, I. N. Lomov, and B. Liu, "Simulation of hypervelocity penetration in limestone," *Int. J. Impact Eng.*, vol. 33, nos. 1–12, pp. 45–52, Dec. 2006.

[12] W. Mingyang, Y. Songlin, L. I. Haibo, Q. Yanyu, and L. I. Jie, "An equivalent calculation method of ground shock effects of hypervelocity projectile striking on rock," *Chin. J. Rock Mech. Eng.*, to be published.
[13] Y. Cheng, M. Wang, C. Shi, H. Fan, L. Li, and Q. Zheng, "Constraining damage size and crater depth: A physical model of transient crater formation in rocky targets," *Int. J. Impact Eng.*, vol. 81, pp. 50–60, Jul. 2015.
[14] G. Birkhoff, D. P. MacDougall, E. M. Pugh, and S. G. Taylor, "Explosives with lined cavities," *J. Appl. Phys.*, vol. 19, no. 6, pp. 563–582, Jun. 1948.
[15] D. L. Orphal, "Explosions and impacts," *Int. J. Impact Eng.*, vol. 33, nos. 1–12, pp. 496–545, 2006.
[16] W. A. Allen and J. W. Rogers, "Penetration of a rod into a semi-infinite target," *J. Franklin Inst.*, vol. 272, no. 4, pp. 275–284, Oct. 1961.
[17] W. Walters, C. Williams, and M. Normandia, "An explicit solution of the alekseevski-tate penetration equations," *Int. J. Impact Eng.*, vol. 33, nos. 1–12, pp. 837–846, 2006.
[18] T. Addabbo, A. Fort, M. Mugnaini, E. Panzardi, and V. Vignoli, "A smart measurement system with improved low-frequency response to detect moving charged debris," *IEEE Trans. Instrum. Meas.*, vol. 65, no. 8, pp. 1874–1883, Aug. 2016.
[19] Y.-J. Cho and C.-Y. Kim, "Improvement of noise characteristics by analyzing power integrity and signal integrity design for satellite on-board electronics," *J. Korean Soc. Aeronaut. Space Sci.*, vol. 48, no. 1, pp. 63–72, Jan. 2020.
[20] J. N. Tripathi, R. K. Nagpal, and R. Malik, "Signal integrity and power integrity issues at system level," (in English), *IETE Tech. Rev.*, vol. 29, no. 5, pp. 365–371, Sep./Oct. 2012, doi: 10.4103/0256-4602.103165.
[21] S. W. Guan, C. W. Kuo, C. C. Wang, and T. Kitazawa, "Power and signal integrity co-design for quad flat non-lead package," (in English), *Electron. Lett.*, vol. 48, no. 15, pp. 942–943, Jul. 2012, doi: 10.1049/el.2012.0494.
[22] D. Wojcik and A. Noga, "Power integrity problems of printed circuit board," (in Polish), *Prz. Elektrotechniczny, Article*, vol. 88, no. 2, pp. 14–16, 2012.
[23] N. E. Huang, Z. Shen, S. R. Long, M. C. Wu, H. H. Shih, Q. Zheng, N.-C. Yen, C. C. Tung, and H. H. Liu, "The empirical mode decomposition and the Hilbert spectrum for nonlinear and non-stationary time series analysis," *Proc. Roy. Soc. London. Ser. A, Math., Phys. Eng. Sci.*, vol. 454, no. 1971, pp. 903–995, Mar. 1998.
[24] N. E. Huang, M.-L. Wu, W. Qu, S. R. Long, and S. S. P. Shen, "Applications of Hilbert-huang transform to non-stationary financial time series analysis," *Appl. Stochastic Models Bus. Ind.*, vol. 19, no. 3, pp. 245–268, Jul. 2003, doi: 10.1002/asmb.501.
[25] Z. Wu and N. E. Huang, "Ensemble empirical mode decomposition: A noise-assisted data analysis method," *Adv. Adapt. Data Anal.*, vol. 1, no. 1, pp. 1–41, Jan. 2009, doi: 10.1142/S1793536909000047.
[26] Y.-X. Li and L. Wang, "A novel noise reduction technique for underwater acoustic signals based on complete ensemble empirical mode decomposition with adaptive noise, minimum mean square variance criterion and least mean square adaptive filter," *Defence Technol.*, vol. 16, no. 3, pp. 543–554, Jun. 2020.
[27] C. Bandt and B. Pompe, "Permutation entropy: A natural complexity measure for time series," (in English), *Phys. Rev. Lett.*, vol. 88, no. 1, Apr. 2002, Art. no. 174102, doi: 10.1103/PhysRevLett.88.174102.
[28] Y. X. Li, X. Gao, and L. Wang, "Reverse dispersion entropy: A new complexity measure for sensor signal," (in English), *Sensors*, vol. 19, no. 23, p. 14, Dec. 2019, Art. no. 5203.
[29] E. Bogatin, *Signal and Power Integrity—Simplified*. Upper Saddle River, NJ, USA: Prentice-Hall, 2010.

DEBIAO ZHANG was born in Jiaxiang, Shandong, China, in June 1989. He is currently pursuing the Ph.D. degree in instrument science and technology with the School of Instrument and Electronics, North University of China. His research interests include circuits and systems, signal acquisition, and dynamic testing techniques in complex and harsh environments.

JIE LI was born in Shanxi, China, in 1976. He received the Ph.D. degree in navigation, guidance, and control from the Department of Automatic Control, Beijing Institute of Technology, Beijing, China, in 2005. From April 2006 to June 2009, he was a Postdoctoral Research Associate with the North University of China, Taiyuan, China, where he works on navigation, guidance, and control. Since 2007, he has been with the School of Instrument and Electronics, North University of China, first as an Associate Professor and then as a Professor, since 2013. His current research interests include strapdown inertial navigation, integrated navigation, and intelligent information processing.

XIAOKAI WEI was born in the Nei Monggol, China, in 1992. He received the B.E. degree in weapon system and launch engineering from the College of Mechatronics Engineering, North University of China, Taiyuan, China, in 2015, where he is currently pursuing the Ph.D. degree in instrument science and technology. His current research interests include inertial navigation, integrated navigation, and adaptive control.

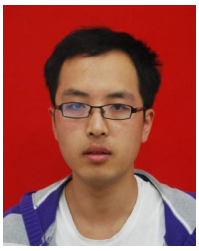

KAIQIANG FENG was born in Shanxi, China, in 1989. He received the B.E. degree from the School of Instrument and Electronics, North University of China, Taiyuan, China, in 2013, where he is currently pursuing the Ph.D. degree in navigation, guidance, and control. His current research interests include inertial navigation, inertial-based integrated navigation systems, and state estimation theory.

YU WANG was born in Shanxi, China, in 1991. He received the B.S. degree from the Inner Mongolia University of Science and Technology, Inner Mongolia, in 2015. He is currently pursuing the Ph.D. degree with the North University of China. His current research interests include magnetically confined plasma and dynamic test.

JIHE ZHAO was born in Hebei, China, in 1995. He is currently pursuing the master's degree in instrument science and technology with the North University of China, where he works on high-speed data recorders.

DONG XUE was born in Liulin, Shanxi, China, in August 1996. He is currently pursuing the master's degree in instrument science and technology with the School of Instrument and Electronics, North University of China. His current research interests include circuits and systems and high-speed data transmission and storage.